PCCP

ROYAL SOCIETY OF CHEMISTRY

PAPER

View Article Online
View Journal | View Issue

Cite this: *Phys. Chem. Chem. Phys.*, 2025, **27**, 24607

Fluorescence excitation and dispersed fluorescence spectra of iso-quinolinyl radicals 4-, 5-, and 8-iso-HC_9H_7N isolated in solid *para*-hydrogen

Chun-Kai Chen,[a] Isabelle Weber, *[a] Qin Yang [b] and Yuan-Pern Lee *[ac]

Received 7th September 2025,
Accepted 4th October 2025

DOI: 10.1039/d5cp03455h

rsc.li/pccp

Nitrogen-substituted polycyclic aromatic hydrocarbons and their derivatives have been proposed as possible carriers of the unidentified infrared emission feature near 6.2 μm in astronomical observations and might also contribute to the diffuse interstellar bands (DIB). We present the previously unobserved dispersed fluorescence and fluorescence excitation spectra of three isomers of hydrogenated iso-quinoline, iso-quinolinyl radicals (iso-HC_9H_7N), isolated in solid *para*-hydrogen (*para*-H_2). The three observed progressions, originating at 18 492, 19 430, and 18 688 cm^{-1} and exhibiting distinct fluorescence lifetimes, are assigned to the D_1–D_0 electronic transitions of the 4-, 8, and 5-iso-HC_9H_7N isomers, respectively. Assignments are supported by Franck–Condon Herzberg–Teller simulations based on (TD-)uB3PW91/6-311++G(2d,2p) optimized geometries and scaled harmonic vibrational frequencies. The dispersed fluorescence and fluorescence excitation spectra predominantly involve vibrational normal modes of a′ symmetry. We compare our spectra to previously reported IR spectra and discuss how the position of hydrogenation influences vibronic structure. The potential contribution of 4-, 8, and 5-iso-HC_9H_7N to the DIB spectrum is discussed.

1. Introduction

Since the discovery of the first diffuse interstellar bands (DIB) by Heger in 1922,[1] over 500 DIB, *i.e.* absorption bands of interstellar origin observed spanning the spectral range from the near infrared (NIR) to the ultraviolet (UV), have been catalogued.[2–4] Yet, the carriers responsible for these bands remain largely unidentified, due to the limited availability of laboratory reference spectra suitable for comparison to astronomical observations. To date, only the buckminsterfullerene cation C_{60}^+ has been conclusively identified as the carrier of five DIB in the NIR.[5,6] Polycyclic aromatic hydrocarbons (PAH) and their protonated, hydrogenated, and cationic derivatives are considered promising candidates for the carriers of DIB.[7,8] They are also generally accepted to contribute to the unidentified infrared (UIR) emission bands at 3.3, 6.2, 7.7, 8.6, 11.2, and 12.7 μm.[9–11] Variations in the line shape of the 6.2-μm band observed, for instance, in the Spitzer/IRS spectra of starburst dominated galaxies[12] suggest a potential role for nitrogen-substituted PAH (PANH) and their derivatives.[13,14] PANH have previously been detected in samples from the Murchison meteorite.[15,16] If PANH contribute to the UIR bands and are present in meteorites, they might also be DIB carriers. However, electronic absorption spectra of PANH and their derivatives at low temperatures have scarcely been recorded, and, to the best of our knowledge, no such spectra have been reported for hydrogenated PANH to date.

The low vapor pressures of large PAH and PANH pose significant challenges for obtaining their gas-phase electronic spectra. Unlike their protonated counterparts, hydrogenated PAH and PANH cannot be stored in cryogenic ion-traps, and their low-temperature gas-phase spectra have rarely been reported. Matrix isolation techniques provide an alternative, as they require lower sample concentrations and allow the matrix to be maintained at temperatures relevant to interstellar conditions. Depending on the matrix host, the preparation of radicals or ions in matrices can be relatively straightforward. Interactions between the matrix host and the isolated guest molecules, however, can induce substantial spectral shifts: matrix shifts up to several hundred wavenumbers have been reported for electronic transitions of molecules isolated in solid rare gases.[17,18] In contrast, the quantum solid *para*-hydrogen (*para*-H_2) is soft and interacts with guest molecules only weakly.

[a] *Department of Applied Chemistry and Institute of Molecular Science, National Yang Ming Chiao Tung University, Hsinchu 300093, Taiwan. E-mail: yplee@nycu.edu.tw; Fax: +886-3-5713491; Tel: +886-3-5131459*
[b] *Institute of Organic Chemistry and Biochemistry, Academy of Sciences, Flemingovonáměstú 2, 16610 Prague, Czech Republic*
[c] *Center for Emergent Functional Matter Science, National Yang Ming Chiao Tung University, Hsinchu 300093, Taiwan*

Protonated molecules can be conveniently prepared by proton-transfer reaction from H_3^+, which can be generated *in situ* by electron bombardment of *para*-H_2. Corresponding hydrogenated molecules are coproducts in this process through either neutralization of protonated species or reactions of the parent molecule with H atoms, a side product of H_3^+ generation. Infrared (IR) absorption spectra of PAH, PANH, and their protonated and mono-hydrogenated derivatives, produced from electron bombardment of *para*-H_2 matrices containing trace PAH or PANH, mostly exhibit narrow line widths and small matrix shifts, typically $<1\%$, induced by the solid *para*-H_2 environment.[19–21] Despite these advantages, *para*-H_2 matrix-isolation spectroscopy has rarely been applied to study electronic transitions. In recent years, we have recorded dispersed fluorescence and fluorescence excitation spectra of several PAH and their protonated and hydrogenated derivatives containing ≤ 42 carbon atoms in *para*-H_2 matrices and found less-divergent and consistent red shifts relative to the gas-phase, compared to Ne and Ar matrices.[22–25] PANH and their derivatives, however, have not yet been examined under similar conditions in our studies.

Quinoline (C_9H_7N) and iso-quinoline (iso-C_9H_7N), the smallest members of the PANH family, are depicted in Fig. 1. As core structural motifs in iso-quinoline alkaloids such as morphine and DTC (*d*-tubercurarine chloride), iso-quinoline has long been of interest in organic, bioorganic, and pharmaceutical synthesis and analysis.[26] Recently, with the growing interest in molecular hydrogen as a clean energy carrier and an alternative to fossil fuels, iso-C_9H_7N, C_9H_7N, and their substituted derivatives have attracted increasing attention as potential liquid organic hydrogen carriers (LOHC). In LOHC, molecular hydrogen is stored and released through catalytic hydrogenation and dehydrogenation of H_2-lean and H_2-rich molecular pairs. The efficiency of hydrogen storage and retrieval depends on the thermodynamic properties of these molecular systems and the availability of suitable catalysts, resulting in an increased interest in the properties of partially and per-hydrogenated PANH.[27–29] Despite this relevance, spectral studies of these molecules remain limited.

To the best our knowledge, the only study of mono-hydrogenated iso-quinoline, iso-HC_9H_7N, is from our laboratory. In two types of experiments, Joshi *et al.*[30] prepared various isomers of iso-HC_9H_7N in solid *para*-H_2 either by electron bombardment or by reacting iso-C_9H_7N with H atoms generated from the reaction of Cl atoms with vibrationally excited H_2.

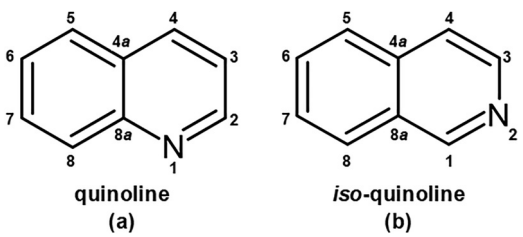

Fig. 1 Molecular structures and skeleton-atom numbering of the two smallest PANH quinoline (C_9H_7N (a)) and iso-quinoline (iso-C_9H_7N (b)).

The recorded IR absorption features were grouped according to their behaviour upon secondary photo-irradiation at various wavelengths between 365 and 553 nm and assigned to eight isomers of iso-HC_9H_7N according to comparison with density functional theory (DFT) calculations. Hydrogenation on the N atom and on all accessible carbon atoms except two at the bridged sites 4a and 8a (Fig. 1) was observed. According to the potential energy scheme (PES) computed at the CCSD(T) level, iso-C_9H_7NH (or 2-iso-HC_9H_7N, hydrogenation at the N-site) has the lowest relative energy. Isomers 5-, 4-, 8, and 1-iso-HC_9H_7N lie within 6 kJ mol^{-1}, whereas 3- and 6-iso-HC_9H_7N have much larger energies, 22–24 kJ mol^{-1} above iso-C_9H_7NH.

We extend our study of the electronic spectra of PAH and their derivatives isolated in solid *para*-H_2 to hydrogenated iso-quinoline and present dispersed fluorescence and fluorescence excitation spectra of three isomers, 4-iso-HC_9H_7N, 5-iso-HC_9H_7N, and 8-iso-HC_9H_7N, characterized by three distinct progressions originating at 18 492, 18 688, and 19 430 cm^{-1}, respectively, with fluorescence lifetimes of $\sim$6, $<$50, and $\sim$105 ns. Spectral assignments are derived from a comparison to vibrationally resolved electronic absorption and emission spectra simulated using a Franck–Condon Herzberg–Teller approach on the basis of quantum-chemically optimized geometries and scaled harmonic vibrational frequencies. In general, the spectra are mostly composed of vibrational normal modes of a′ symmetry. The dispersed fluorescence spectra are compared with the IR absorption spectra of the same isomers in solid *para*-H_2 reported by Joshi *et al.*,[30] and spectral differences are discussed. A brief comparison to astronomical DIB data is provided.

2. Experimental and computational methods

The *para*-H_2/laser-induced fluorescence experiment has been described in detail elsewhere;[23,31] therefore, only a brief overview is given here. The substrate, a nickel-coated copper flat mounted onto the second stage of a closed-cycle helium refrigerator, is cooled to $\sim$3.5 K and serves as the reflective surface for spectroscopy.

Para-H_2 was prepared by passing *normal*-H_2 (Chiah-Lung, purity 99.9999%) over a Fe(III) oxide catalyst cooled to $\sim$13 K; the minimum mole fraction of *ortho*-H_2 achievable at this temperature is $\sim$100 ppm. Due to the low vapour pressure of iso-C_9H_7N, preparing pre-mixed C_9H_7N/*para*-H_2 samples was not feasible. Instead, a small flow of *para*-H_2 (flow rate $\sim$15 STP L min^{-1}, in which STP stands for standard temperature at 273 K and pressure at 760 torr) was passed over the liquid sample, which was purified through three freeze–pump–thaw cycles prior to use, maintained at room temperature. To produce hydrogenated iso-HC_9H_7N, the sample mixture was bombarded during deposition with an electron beam at 270 eV and 8 μA, generated by an electron gun (Kimball Physics, EPG-7). A typical deposition lasted 5–6 h. Matrix deposition was monitored with a Fourier-transform infrared spectrometer

(FTIR, Bruker, iFS66v) equipped with a KBr beam splitter and a Hg–Cd–Te (MCT) detector cooled to 77 K. IR spectra were typically acquired over 300 scans and covered the range 500–4500 cm^{-1} at a resolution of 0.25 cm^{-1}.

To record dispersed fluorescence spectra, we irradiated the matrix with the output of an optical parametric oscillator (OPO, EKSPA NT340) laser, pumped by the output of a frequency-tripled Nd:YAG laser (EKSPLA, NT300) operating at 10 Hz. The OPO laser beam was expanded to a diameter of $\sim$1.5 cm with a telescope to maximize the overlap with the sample; the laser energy at the entrance window was $\sim$1 mJ. Emission from the matrix was collected with a convex lens and a collimator, coupled into an optical fiber, and transmitted to the spectrograph consisting of a monochromator (Andor Shamrock SR500i, focal length 0.5 m) and an intensified charge-coupled device (iCCD, Andor iStar DH320T-18U-73, 1024 $\times$ 225 pixels, pixel size 26 μm $\times$ 26 μm). We employed a 600 grooves per mm grating blazed at 500 nm and, for the recording of dispersed fluorescence spectra, a monochromator entrance slit width of 22 μm, resulting in a linear dispersion of 3.33 nm mm^{-1}; in this configuration, each pixel of the iCCD corresponds to 0.086 nm. Dispersed fluorescence spectra were corrected for wavelength-dependent variations in grating efficiency and iCCD photocathode quantum efficiently. Wavelengths were calibrated with low-pressure Hg, Ne, and Kr lamps. Fluorescence excitation spectra were acquired by stepping the excitation laser wavelength in increments of 0.1 nm, corresponding to 4.9–3.3 cm^{-1} across the range 450–550 nm, while probing fluorescence emission in a specific wavelength range. In the spectral range covered, the spectral linewidth of the OPO output is <4 cm^{-1}. Laser-induced fluorescence (LIF) experiments were typically conducted over 2–3 days and no significant changes in signal intensities in the recorded dispersed fluorescence spectra were observed over this period.

Quantum-chemical calculations were performed with the Gaussian 16 program package, Revision B.01.[32] We computed optimized geometries and harmonic vibrational frequencies of the electronic ground state (D_0) and electronically excited states with the uB3PW91/6-311++G(2d,2p) and TD-uB3PW91/6-311++G(2d,2p) methods, respectively. To simulate vibrationally resolved electronic absorption and emission spectra, we employed a Franck–Condon Herzberg–Teller approach;[33] the computed stick spectra were convoluted with Gaussian line shapes with full-width at half-maximum (FWHM) selected to match with the experimental spectra. For 1-iso-HC_9H_7N, the vibrationally-resolved absorption and emission spectra were calculated with a local modified version of Gaussian to achieve a higher progression by using internal coordinates and reduced dimensionality schemes.[34,35] Harmonic vibrational wavenumbers were scaled by 0.978 to account for systematic deviations in the calculations. This scaling factor was derived from a comparison between vibrational frequencies computed at this level of theory and the IR spectra of selected PAH isolated in solid *para*-H_2 in previous studies.[23] Due to the lack of independent experimental vibrational frequencies for electronically excited states, the determination of a separate scaling factor for excited-state vibrational frequencies was not possible. We therefore applied the same scaling factors to harmonic wavenumbers of both ground and excited states. Our previous studies support this approach: for *peri*-HBC,[22] the mean absolute deviations in peak positions inferred from fluorescence excitation spectra and theoretical predictions at the B3PW91/6-311++G(2d,2p) level was 8 $\pm$ 6 cm^{-1}.

3. Results and discussion

3.1. Quantum-chemical calculations

Hydrogenation of iso-C_9H_7N can proceed at ten distinct atomic sites, as indicated in Fig. 1. Among these ten possible isomers, iso-C_9H_7NH, formed *via* H-atom addition to the N atom, is the most stable. In contrast, the two isomers 4a- and 8a-iso-HC_9H_7N, resulting from H-atom addition to the bridging C atoms, exhibit the highest relative energies of +100 and +91 kJ mol^{-1}, respectively.[30] Oscillator strength (f) and vertical absorption and emission energies corresponding to the transition between the electronic ground state (D_0) and the first electronically excited state (D_1) of the eight most stable isomers calculated with the TD-uB3PW91/6-311++G(2d,2p) method are summarized in Table 1; their simulated $D_1 \rightarrow D_0$ emission spectra except 1-iso-HC_9H_7N, are compared in Fig. 2(d)–(j).

According to the simulations, the most intense peak in the depicted spectra corresponds to the vibrationless origin. Vibronic bands are less intense, with maximum intensities $<45\%$ relative to the origin band. In the D_0 state, the ring-skeleton is planar, and, for most isomers except 1-iso-HC_9H_7N, this planarity is preserved upon excitation to the D_1 state. Consequently, their vibronic spectra are composed mainly of a′-symmetric vibrational normal modes and their combination bands. For 2-iso-HC_9H_7N (iso-C_9H_7NH), our calculations predict a slight out-of-plane deformation of the ring-skeleton, as indicated by planarity indices[22,36] of 2.2 and 0.2 for the N-substituted and all-C-ring moieties, respectively, resulting in lower intensities in the vibronic spectrum and vibrational progressions extending up to $\sim$5000 cm^{-1}.

In contrast, for 1-iso-HC_9H_7N, TD-DFT calculations predict substantial deformation of the ring-skeleton of the optimized

Table 1 Relative energies of various iso-HC_9H_7N isomers, vertical absorption and emission wavelengths, and vertical absorption oscillator strengths f of their D_1–D_0 transitions and D_1 spin contamination $\langle S^2 \rangle$

		TD-uB3PW91/6-311++G(2d,2p)			
	Rel. energy[a]/kJ mol^{-1}	ΔE_{abs}^{vert}/nm	ΔE_{emi}^{vert}/nm	f	$\langle S^2 \rangle$
1	6	525.30	1179.79	0.001	0.842
2	0	839.58	2268.43	0.001	0.837
3	22	514.06	664.25	0.004	0.895
4	3	447.47	522.88	0.025	0.907
5	2	448.55	528.04	0.006	0.890
6	24	498.47	592.81	0.005	1.025
7	24	539.75	703.92	0.007	0.951
8	3	432.48	483.62	0.006	0.880

[a] Relative energies reported by Joshi *et al.*,[30] computed at the CCSD(T)/6-311++G(d,p)//B3LYP/6-311++G(d,p) level.

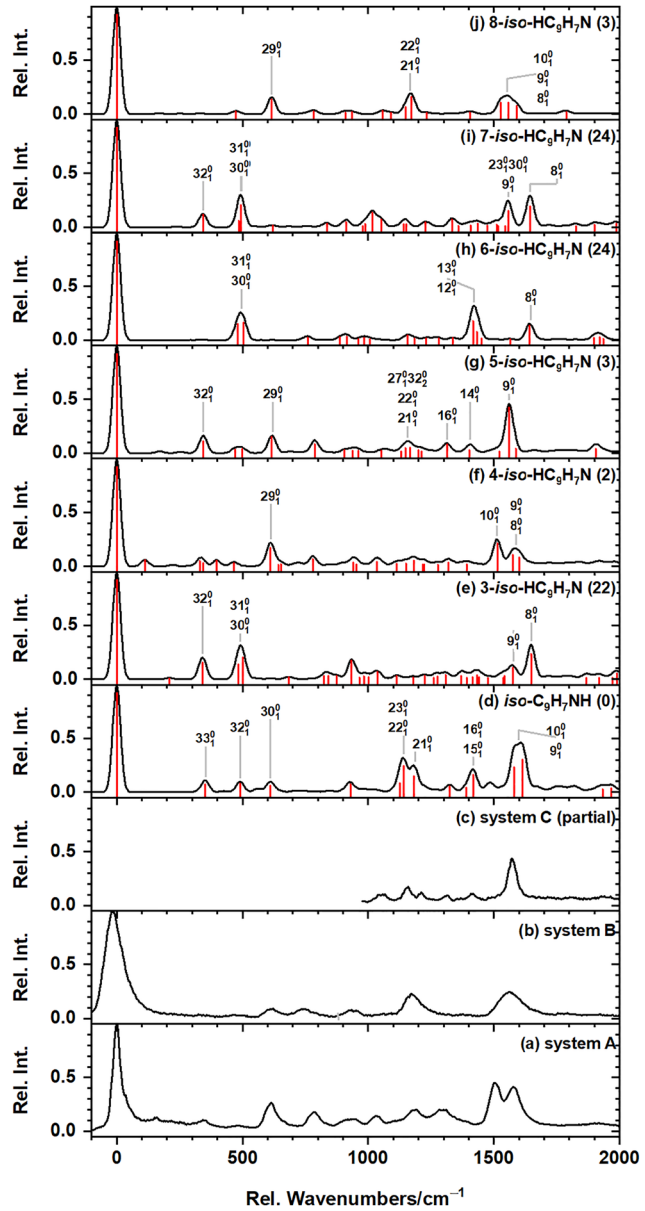

Fig. 2 Comparison of observed dispersed fluorescence spectra with simulated $D_1 \rightarrow D_0$ emission spectra of various isomers of hydrogenated iso-quinoline. (a) Experimental system A, (b) Experimental system B, and (c) Experimental system C (partial). Simulated emission spectra of various isomers of iso-HC_9H_7N are shown in (d)–(j). To facilitate direct comparison, all spectra were shifted to align their 0_0^0 bands and the computed Franck–Condon Herzberg–Teller stick spectra were convoluted with a Gaussian line shape function with a full-width half-maximun (FWHM) of 35 cm^{-1}. Relative energies in kJ mol^{-1} are given in parentheses. The origin bands of the experimental spectra are located at 18 492 cm^{-1} (system A), 19 430 cm^{-1} (system B), and 18 688 cm^{-1} (system C, not shown).

D_1 geometry, as shown in Fig. S1 (SI). The N-substituted ring has a planarity index of 28.2, whereas the all-C ring has a planarity index of 3.9. Due to the pronounced geometric disparity between D_1 and D_0, Franck–Condon factors for fundamental vibrational normal modes and first-order overtone and combination bands are small, and the Franck–Condon Herzberg–Teller algorithm, implemented in Gaussian 16, Revision B.01,[32] fails to converge. Consequently, no simulated $D_1 \rightarrow D_0$ emission spectrum of 1-HC_9H_7N is depicted in Fig. 2. With new definitions of internal coordinates and a reasonable reduced dimensionality, we achieved a final spectral progression of 78% (original calculation yielded 0.01%) for the $D_1 \rightarrow D_0$ emission spectrum of 1-iso-HC_9H_7N and obtained the spectrum depicted in Fig. S2 (SI). The high periodicity of the spectral structure and the substantially reduced line density, when additional six vibrational normal modes are omitted, reflect the significant change in geometry predicted for the D_1–D_0 transition at this level of theory; the dominance of long progressions of overtone and combination bands was observed.

Although the vibronic patterns in Fig. 2(d)–(j) vary considerably depending on the position of H addition, several notable trends emerge. Contributions of vibrational normal mode in the observed transitions are discussed in detail in Section SA (SI).

3.2. Dispersed fluorescence of 4-iso-HC_9H_7N and 8-iso-HC_9H_7N

Upon excitation at 497.0 (20 120 cm^{-1}) and 475.0 nm (21 053 cm^{-1}) of a matrix of iso-C_9H_7N in solid *para*-H_2 deposited under electron bombardment, two distinct emission patterns were observed with most intense features at 18 492 cm^{-1} (540.8 nm; system A) and 19 430 cm^{-1} (514.7 nm; system B), as shown in Fig. 2a and b, and also in Fig. S5 (SI). To determine their lifetimes, we probed temporal profiles of fluorescence emission and fitted the decay curves with a mono-exponential decay function $y(t) = y_0 + A \times \exp(-\tau/t)$, in which τ denotes the excited-state lifetime (Fig. S6, SI). System A exhibits a fluorescence lifetime of $\sim$6 ns, whereas system B yields a longer lifetime of 104 $\pm$ 3 ns, indicative of two distinct electronic transitions.

The observed dispersed fluorescence spectra are compared with simulated $D_1 \rightarrow D_0$ emission spectra of various hydrogenated iso-quinoline isomers in Fig. 2. To facilitate comparison, all simulated vibronic stick spectra were shifted to align their 0_0^0 bands and convoluted with a Gaussian lineshape (FWHM of 35 cm^{-1}). Characteristic of system A are two intense and partially unresolved features at 1507 and 1577 cm^{-1}, with relative intensities of 45 and 41% compared to the 0_0^0 band, respectively. A moderately intense feature at 615 cm^{-1} with a relative intensity of $\sim$25% also appeared, alongside five weaker bands (<20%) located between 615 and 1500 cm^{-1}. System B displays two characteristic bands $\sim$1175 and 1570 cm^{-1}, both with relative intensities of $\sim$24%, accompanied by three weaker features below 1000 cm^{-1} with relative intensities under 10%.

The simulated $D_1 \rightarrow D_0$ emission spectra of 3-, 4-, and 7-iso-HC_9H_7N all exhibit a characteristic double-peak structure in region 1500–1600 cm^{-1}, as observed in system A. However, only the simulated spectrum of 4-iso-HC_9H_7N reproduces the relative intensities of these two peaks in the experimental spectrum. Furthermore, in the 500–1500 cm^{-1} region, the most intense peak in the simulated spectrum of 4-iso-HC_9H_7N

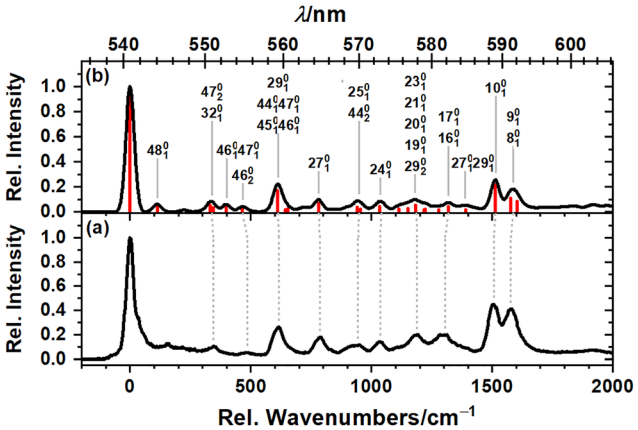

Fig. 3 Comparison of observed and simulated dispersed fluorescence spectra of 4-iso-HC_9H_7N. (a) Dispersed fluorescence spectrum of 4-iso-HC_9H_7N isolated in solid *para*-H_2 recorded upon excitation at 20 120 cm^{-1} (497.0 nm). The bottom axis denotes the displacement from the orgin band, observed at 18 492 cm^{-1} (540.8 nm), while the top axis represents the wavelength of the observed spectrum. (b) The $D_1 \rightarrow D_0$ emission spectrum simulated by convolution the Franck–Condon Herzberg–Teller stick spectrum (red) with a Gaussian line shape of FWHM 40 cm^{-1}; vibrational wavenumbers were scaled by 0.978. Vibrational mode assignments are indicated.

appears near 617 cm^{-1} (rel. int. ~25%), consistent with experiments, and the remaining spectral features are also consistent with our experimental data. In contrast, the simulated spectra of 3- and 7-iso-HC_9H_7N both show features near 495 and 350 cm^{-1} with relative intensities of 35 and 20%, but lack any prominent feature near 615 cm^{-1}. We therefore assign the dispersed fluorescence spectrum originating at 18 492 cm^{-1} (system A) to the $D_1 \rightarrow D_0$ transition of 4-iso-HC_9H_7N in solid *para*-H_2.

Detailed vibrational assignments for the dispersed fluorescence spectrum of 4-iso-HC_9H_7N isolated in solid *para*-H_2, derived on comparison with simulations, are presented in Fig. 3 and Table 2. The relative intensities and peak positions show satisfactory agreement, with an average absolute deviation of 8 ± 6 cm^{-1}, comparable to our results for the 1-hydronaphthyl radical (1-$C_{10}H_9$) in solid *para*-H_2.[24] Most features are assigned to vibrational normal modes of a′ symmetry, consistent with the preservation of ring-skeleton planarity and the symmetric deformation of the HCH angle and C–H bond lengths in the CH_2 moiety upon excitation to the D_1 state. The predicted weak contributions from overtone and combination bands, either involving a′ vibrations or two quanta of a″ vibrations (ν_{45}–ν_{48}), are consistent with the allowed transitions governed by symmetry operations of the point group C_s.

The IR spectrum of 4-iso-HC_9H_7N in solid *para*-H_2 has previously been reported by Joshi *et al.*[30] Consistent with the low molecular symmetry of the radical (point group C_s), all vibrational normal modes are symmetry allowed and may contribute to both IR and LIF spectra, although their intensities might differ depending on the governing rules for electronic and vibronic transitions. In electronic spectra, the intensities of individual vibrational modes are determined by their

Table 2 Assignments of peaks in the dispersed fluorescence spectrum of 4-iso-HC_9H_7N isolated in solid *para*-H_2

para-H_2		uB3PW91				
IR[a]/ cm^{-1}	LIF[b]/ cm^{-1}	FCHT[c]/ cm^{-1}	Rel. int.[d]/ %	Scaled[e]/ cm^{-1}	Assignment	Sym.
	0	0	100	0	0_0^0	a′
		113	5.9	(112)	48_2^0	a′
	344	336	5.1	(331)	47_2^0	a′
			3.3	344	32_1^0	a′
		399	5.6	(398)	$46_1^0 47_1^0$	a′
	486	466	3.0	(465)	46_2^0	a′
	615	610	17.3	612	29_1^0	a′
			1.5	(642)	$44_1^0 47_1^0$	a′
			2.2	(653)	$45_1^0 46_1^0$	a′
(748.1)			(<0.1)	742	40_1^0	a″
	786	778	7.0	780	27_1^0	a′
	945	943	3.5	940	25_1^0	a
			2.0	(953)	44_2^0	a′
	1036	1037	4.2	1034	24_1^0	a′
	1188	1181	2.4	1113	23_1^0	a′
			2.6	1151	21_1^0	a′
			5.4	1183	20_1^0	a′
			1.9	1217	19_1^0	a′
			2.2	(1223)	29_2^0	a′
(1245.9)			(<0.1)	1247	18_1^0	a′
1269.4	1304	1318	1.6	1277	17_1^0	a′
			4.0	1320	16_1^0	a′
		1389	1.8	(1391)	$27_1^0 29_1^0$	a′
(1483.7)			(0.8)	1486	11_1^0	a′
	1507	1514	21.8	1513	10_1^0	a′
	1577	1584	10.7	1576	9_1^0	a′
			8.3	1602	8_1^0	a′
(3087.9)			(<0.1)	3132	1_1^0	a′

[a] Peak positions in the IR absorption spectrum of 4-*iso*-HC_9H_7N isolated in solid *para*-H_2 reported by Joshi *et al.*[30] Values in parentheses represent modes predicted by the Frank–Condon Herzberg–Teller (FCHT) simulations with a relative intensity of <1.5% in the simulated LIF spectrum. [b] Vibrational spacing relative to the origin band at 18 492 cm^{-1} (540.8 nm). [c] Vibrational spacings from the convoluted simulated stick spectrum calculated with the FCHT method. [d] Intensities relative to the most intense peak (0_0^0 band). Only vibrational modes with relative intensities ≥1.5% are listed. The weak features corresponding to IR absorption bands reported by Joshi *et al.*[30] are listed in parentheses. [e] Harmonic vibrational wavenumbers scaled by a factor of 0.978. Values given in parentheses for combination and overtone bands are the sum of the fundamentals.

Franck–Condon factors, which are more pronounced for vibrational modes reflecting geometry changes induced by electronic transition. Since the planarity of the ring-skeleton is retained upon electronic excitation, intense features observed in the dispersed fluorescence spectra are predominantly associated with vibrational normal modes of a′ symmetry. Conversely, peak intensities in IR spectra are governed by the change in dipole moment induced by the vibrational motion, and, in consequence, the most intense IR bands (ν_{40}) are associated with vibrational modes of a″ symmetry.

Joshi *et al.*[30] identified five IR lines of 4-iso-HC_9H_7N in solid *para*-H_2 and assigned them to ν_1 (a′), ν_{11} (a′), ν_{17} (a′), ν_{18} (a′), and ν_{40} (a″); other IR lines predicted to have significant intensities were interfered by either iso-C_9H_7N or other isomers of iso-HC_9H_7N. Among these modes, our simulations predict

that only ν_{17} (a′) and ν_{11} (a′) contribute weakly to the electronic emission spectrum, with intensities 1.6 and 0.8% of the most intense feature 0_0^0, respectively (Table 2). The band at 1304 cm^{-1} in the dispersed fluorescence spectrum is predicted to be a superposition of ν_{17} (1277 cm^{-1}, a′) and ν_{16} (1320 cm^{-1}, a′), with relative intensities 1.6 and 4.0%, respectively, resulting in an effective peak position at 1308 cm^{-1}. The corresponding peak in the IR spectrum of 4-iso-HC_9H_7N in solid *para*-H_2 at 1269.4 cm^{-1} is assigned to only ν_{17}, with no contribution from ν_{16}, explaining the large deviation between the two spectra.

For system B, among all simulated spectra, only the simulated $D_1 \rightarrow D_0$ emission spectrum of 8-iso-HC_9H_7N exhibits two pes of comparable intensity (~22%) near 1178 and 1567 cm^{-1}, similar to the experimental spectrum. A third, weaker feature (rel. intensity ~15%) is predicted near 620 cm^{-1} and also observed in the experimental spectrum, albeit with slightly lower intensity (~9%); other predicted features are generally in agreement with the experimental data. The only other isomer whose simulated $D_1 \rightarrow D_0$ spectrum displays characteristic features near 1180 and 1580 cm^{-1} is iso-C_9H_7NH, the lowest-energy isomer. In this case, however, the two bands are predicted with much higher relative intensities (~63 and ~40%, respectively), and the predicted bands near 355, 490, and 1420 cm^{-1} were not observed in our experiments.

Therefore, we assign system B, with an origin at 19 430 cm^{-1}, to the $D_1 \rightarrow D_0$ transition of 8-iso-HC_9H_7N in solid *para*-H_2. A contribution from protonated iso-C_9H_7N to either spectrum is unlikely because our calculations predict the S_1–S_0 transition of iso-$C_9H_7NH^+$, the lowest-energy protonated isomer and the only one observed previously in IR absorption in solid *para*-H_2,[30] to occur at 376.6 nm with an oscillator strength f = 0.442. Joshi *et al.* differentiated protonated and hydrogenated iso-C_9H_7N based on their behavior over time: recombination of iso-$C_9H_7NH^+$ with solvated electrons in the *para*-H_2 matrix resulted in a decrease in iso-$C_9H_7NH^+$ and an increase in iso-HC_9H_7N. No decrease in intensities in the dispersed fluorescence spectra were observed over the experimental runtime of 2–3 days, supporting that iso-$C_9H_7NH^+$ is unlikely to contribute to the observed spectra.

Detailed vibrational assignments for the dispersed fluorescence spectrum of 8-iso-HC_9H_7N isolated in solid *para*-H_2, derived on comparison with the simulations, are presented in Fig. 4 and Table 3. The simulated and observed peak positions and relative intensities are in satisfactory agreement, with an absolute average deviation 6 ± 4 cm^{-1}. As discussed above for 4-iso-HC_9H_7N, most of the observed peaks are assigned to vibrational normal modes of a′ symmetry.

For 8-iso-HC_9H_7N, Joshi *et al.*[30] assigned nine IR vibrational lines to two C–H stretching modes ν_1 (a′) and ν_2 (a′), five C–C and C–N stretching modes ν_8 (a′), ν_{11} (a′) and ν_{12} (a′), ν_{18} (a′), ν_{25} (a′), and two out-of-plane vibrations ν_{39} (a″) and ν_{42} (a″). Of these, only ν_{25} (a′) and ν_8 (a′) are predicted to contribute to the $D_1 \rightarrow D_0$ emission spectrum, with relative intensities of 1.7 and 7.8%, respectively.

A notable distinction between the dispersed fluorescence spectra of 4- and 8-iso-HC_9H_7N lies in the relative intensities of

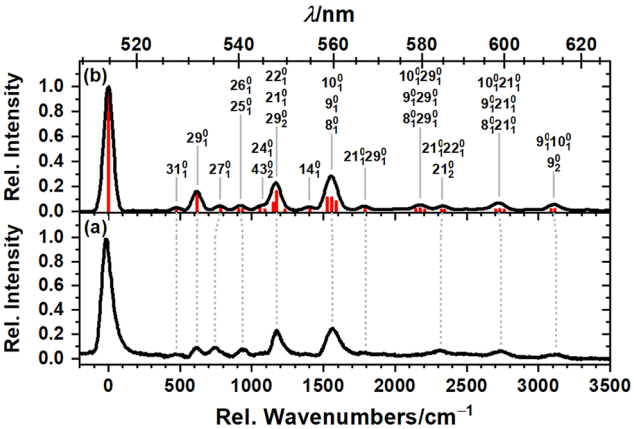

Fig. 4 Comparison of observed and simulated dispersed fluorescence spectra of 8-iso-HC_9H_7N. (a) Dispersed fluorescence spectrum of 8-iso-HC_9H_7N isolated in solid *para*-H_2 recorded upon excitation at 21 053 cm^{-1} (475.0 nm). The bottom axis denotes the displacement from the orgin band, observed at 19 430 cm^{-1} (514.7 nm), while the top axis represents the wavelength of the observed spectrum. (b) The $D_1 \rightarrow D_0$ emission spectrum simulated by convolution the Franck–Condon Herzberg–Teller stick spectrum (red) with a Gaussian line shape of FWHM 75 cm^{-1}; vibrational wavenumbers were scaled by 0.978. Vibrational mode assignments are indicated.

the three a′ symmetric C–C and C–N stretching modes ν_8, ν_9, and ν_{10}. In the simulated D_1–D_0 emission spectrum of 4-iso-HC_9H_7N, their relative intensities follow the order ν_{10} (21.8%) ≫ ν_9 (10.7%) > ν_8 (8.3%), whilst in the simulated D_1–D_0 emission spectrum of 8-iso-HC_9H_7N, ν_{10} and ν_9 exhibit comparable relative intensities – 10.7 and 11.0%, respectively – both exceeding that of ν_8 (7.9%). Atomic displacement vectors induced by these modes are illustrated in Fig. 5. In the 4-iso-HC_9H_7N radical, ν_{10} primarily affects the C–N bond, and, to a lesser extent, the C(8a)–C(1) bond; the C-skeleton of the all-C ring is largely unaffected. On the contrary, ν_9 and ν_8 mostly distort the C-skeleton of the all-C ring, with the largest impact on C(6)-C(7) and C(4a)–C(8a), and C(4a)–C(5) and C(7)–C(8), respectively.

As illustrated in Fig. S4b (SI), the greatest change in bond length upon transition between the D_1 and D_0 in 4-iso-HC_9H_7N occurs at the C–N bond. Among the three pairs of C–C and C–N bonds mostly impacted by the three normal modes ν_8, ν_9, and ν_{10}, the pair C(4a)–C(5) and C(7)–C(8) corresponding to ν_8 is least affected by the electronic transition, consistent with the low intensity of ν_8 predicted in the D_1–D_0 emission spectrum. Changing the hydrogenation site from C(4) to C(8) also changes the displacements associated with the three vibrational normal modes ν_8, ν_9, and ν_{10}: in 8-iso-HC_9H_7N, ν_{10} mainly affects the C(6)–C(7) bond and, to a lesser extent, C(4a)–C(5); ν_9 mainly impacts the C–N and C(4a)–C(8a) bonds, and ν_8 mainly impacts the C(8a)–C(1) and C(3)–C(4) bonds. Similar to the 4-iso-HC_9H_7N radical, the change in bond lengths of 8-iso-HC_9H_7N associated with the D_1–D_0 transition is smallest for the pair of C–C bonds characteristic of ν_8, and the intensity predicted for ν_8 in the emission spectrum is comparably small. The changes in bond lengths of the C(6)–C(7) and the C–N bonds (+3.1 and

Table 3 Assignments of peaks in the dispersed fluorescence spectrum of 8-iso-HC_9H_7N isolated in solid *para*-H_2

para-H_2	uB3PW91					
IR[a]/ cm^{-1}	LIF[b]/ cm^{-1}	FCHT[c]/ cm^{-1}	Rel. int.[d]/ %	Scaled[e]/ cm^{-1}	Assignment	Sym.
	0	0	100	0	0_0^0	a′
	474	473	2.6	472	31_1^0	
	618	618	13.6	616	29_1^0	a′
(653.7)			(<0.1)	648	42_1^0	a″
	743	778	2.6	784	27_1^0	a′
(830.5)			(<0.1)	831	39_1^0	a″
	936	919	1.5	910	26_1^0	a′
941.6			1.7	936	25_1^0	a′
			3.2	1056	24_1^0	a′
			1.2	(1091)	43_2^0	a′
	1174	1166	6.7	1150	22_1^0	a′
			16.2	1173	21_1^0	a′
			1.2	(1232)	29_2^0	a′
(1245.5)			(<0.1)	1264	18_1^0	a′
			1.4	1404	14_1^0	a′
(1432.2)			(<0.1)	1431	12_1^0	a′
(1467.6)			(<0.1)	1473	11_1^0	a′
	1560	1553	10.7	1528	10_1^0	a′
			11.0	1558	9_1^0	a′
1576.2			7.8	1590	8_1^0	a′
	1792	1784	2.0	(1789)	$21_1^0 29_1^0$	a′
		2175	1.7	(2144)	$10_1^0 29_1^0$	a′
			2.4	(2174)	$9_1^0 29_1^0$	a′
			1.2	(2206)	$8_1^0 29_1^0$	a′
	2311	2332	1.0	(2322)	$21_1^0 22_1^0$	a′
			1.3	(2345)	21_2^0	a′
	2737	2723	1.3	(2700)	$10_1^0 21_1^0$	a′
			1.5	(2731)	$9_1^0 21_1^0$	a′
			1.2	(2762)	$8_1^0 21_1^0$	a′
	3124	3106	1.4	(3086)	$9_1^0 10_1^0$	a′
			1.9	(3116)	9_2^0	a′
(3076.6)			(<0.1)	3119	2_1^0	a′
(3083.9)			(<0.1)	3130	1_1^0	a′

[a] Peak positions in the IR absorption spectrum of 8-iso-HC_9H_7N isolated in solid *para*-H_2 reported by Joshi *et al.*[30] Values in parentheses represent modes predicted by FCHT simulations with a relative intensity of <1.5% in the simulated spectrum. [b] Vibrational spacing relative to the origin band at 19 430 cm^{-1} (514.7 nm). [c] Vibrational spacings from the convoluted simulated stick spectrum calculated with the FCHT method. [d] Intensities relative to the most intense peak (0_0^0 band). Only vibrational modes with relative intensities ≥1.5% are listed. The weak features corresponding to IR absorption bands reported by Joshi *et al.*[30] are listed in parentheses. [e] Harmonic vibrational wavenumbers scaled by a ftor 0.978. Values given in parentheses for combination and overtone bands are the sum of the fundamentals.

+3.3%, respectively) in 8-iso-HC_9H_7N are similar, consistent with the comparable intensities of ν_{10} and ν_9 in the simulated D_1–D_0 emission spectrum.

3.3. Fluorescence excitation spectrum of 4-iso-HC_9H_7N

Probing fluorescence emission in the ranges 18 399–18 601 cm^{-1} (537.6–543.5 nm) and 16 787–17 030 cm^{-1} (587.2–595.7 nm), while varying the excitation wavelength at 0.1 nm increments from 490 to 516 nm and 516 to 545 nm, respectively, we obtained the fluorescence excitation spectrum depicted in Fig. 6a. This spectrum consists of a very intense 0_0^0

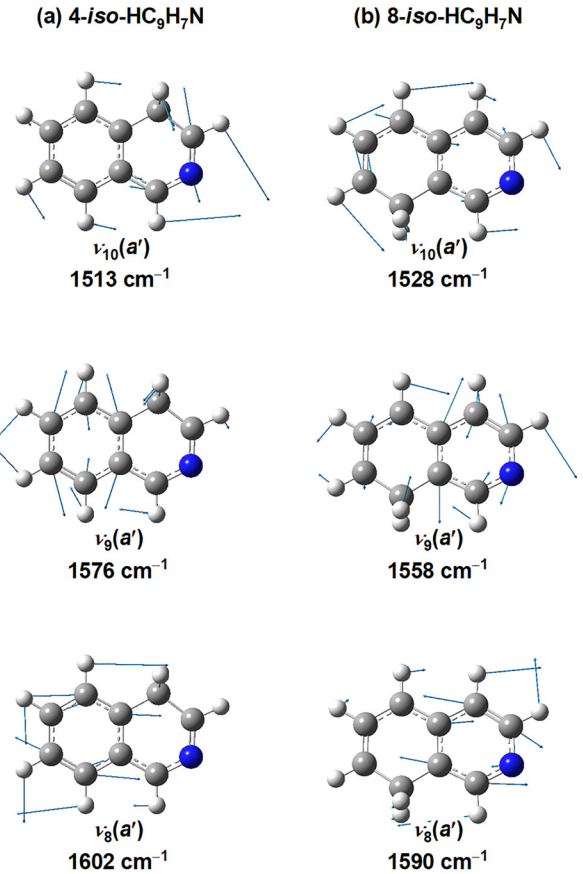

Fig. 5 Displacement vectors induced by the three a′ C–C stretching modes of 4-iso-HC_9H_7N (a) and 8-HC_9H_7N (b) in their electronic ground states calculated at the uB3PW91/6-311++G(2d,2p) level.

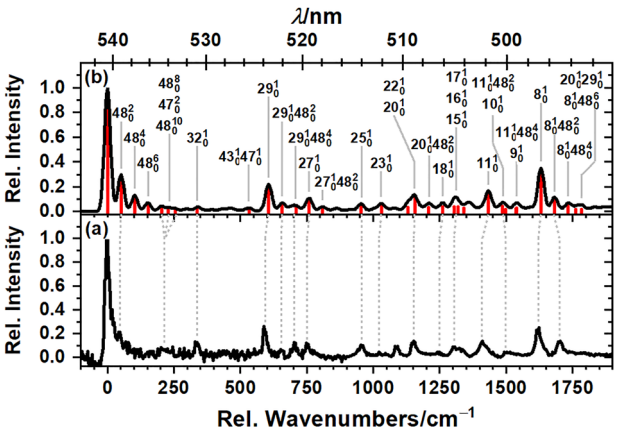

Fig. 6 Comparison of observed and simulated excitation of 4-iso-HC_9H_7N. (a) Fluorescence excitation spectrum of 4-iso-HC_9H_7N isolated in solid *para*-H_2 obtained by probing emission in regions 16 787–17 030 cm^{-1} (<900 cm^{-1}) and 18 399–18 601 cm^{-1} (>900 cm^{-1}). The bottom axis denotes the displacement from the orgin band, observed at 18 495 cm^{-1} (540.7 nm), while the top axis represents the wavelength of the observed spectrum. (b) The $D_1 \leftarrow D_0$ absorption spectrum simulated by convolution the Franck–Condon Herzberg–Teller stick spectrum (red) with a Gaussian line shape of FWHM 25 cm^{-1}; vibrational wavenumbers were scaled by 0.978. Vibrational mode assignments are indicated.

band at 18 495 cm^{-1} (540.7 nm) along with several weaker vibrational bands with relative intensities <25%. The 0_0^0 band closely matches the 0_0^0 band at 18 492 cm^{-1} in the dispersed fluorescence spectrum of 4-iso-HC_9H_7N, shown in Fig. 3a. The probed range 16 787–17 030 cm^{-1} covers the weaker bands of 8_1^0, 9_1^0, and 10_1^0. in the dispersed fluorescence spectrum, whereas the probed range 18 399–18 601 cm^{-1} covers the intense 0_0^0 band. Consequently, the signal-to-noise ratio is superior below 516 nm. According to the overlay of dispersed fluorescence spectra of the three iso-HC_9H_7N isomers recorded in this study and the probed regions shaded in gray (Fig. S7, SI), interferences due to emission of 8-iso-HC_9H_7N and 5-iso-HC_9H_7N are expected to be negligible.

The experimental spectrum is compared with the simulated $D_1 \leftarrow D_0$ absorption spectrum of 4-iso-HC_9H_7N in Fig. 6. Detailed assignments for the observed features are provided in Fig. 6b and Table 4. In general, the experimental and theoretical results are in satfactory agreement, with an average absolute deviation in peak positions of 8 ± 7 cm^{-1}. We also compare this spectrum to the simulated $D_1 \leftarrow D_0$ absorption spectra of various iso-HC_9H_7N isomers in Fig. S8 (SI). The observed excitation spectrum (trace a) agrees with that predicted for 4-iso-HC_9H_7N, but not with predictions for other isomers of iso-HC_9H_7N.

Although both dispersed fluorescence and fluorescence excitation spectra of 4-iso-HC_9H_7N are primarily composed of vibrational normal modes of a′ symmetry, they differ in relative intensities and in the contribution of combination and overtone bands: overtones containing $2n$ quanta of ν_{48} (a″, 26 cm^{-1}) up to n = 5 and their combination bands with intense modes of a′ symmetry are predicted to contribute only to the fluorescence excitation spectrum.

3.4. Fluorescence excitation spectrum of 8-iso-HC_9H_7N

To obtain the fluorescence excitation spectrum of 8-iso-HC_9H_7N, we monitored fluorescence emission in the range 18 103–18 312 cm^{-1} (546.1–552.4 nm), shaded in light red in Fig. S7 (SI), corresponding to a superposition of bands 22_1^0 and 21_1^0 in the dispersed fluorescence spectrum. The signal-to-noise ratio of this excitation spectrum is worse than that of 4-iso-HC_9H_7N, likely due to the oscillator strength predicted for the D_1–D_0 transition of 8-iso-HC_9H_7N being about 1/4 that of 4-iso-HC_9H_7N. This spectrum, depicted in Fig. 7a, consists of an intense 0_0^0 band at 19 433 cm^{-1} (514.6 nm), closely matching the 0_0^0 band at 19 430 cm^{-1} in the dispersed fluorescence spectrum of 8-iso-HC_9H_7N; characteristic vibrational features appeared at 700, 1169, 1532, and 1620 cm^{-1}.

Peak-by-peak assignments, derived *via* comparison with the simulated $D_1 \leftarrow D_0$ spectrum of 8-iso-HC_9H_7N, are listed in Table 5 and indicated in Fig. 7b. Similar to the dispersed fluorescence spectrum, the fluorescence excitation spectrum of 8-iso-HC_9H_7N is also dominated by vibrational normal modes of a′ symmetry. The average absolute deviation in peak positions between experiment and simulation, 8 ± 6 cm^{-1}, is comparable to that derived for 4-iso-HC_9H_7N. We also compare this spectrum with the simulated $D_1 \leftarrow D_0$ absorption spectra of various iso-HC_9H_7N isomers in Fig. S8 (SI). The observed excitation spectrum (trace b) agrees with that predicted for 8-iso-HC_9H_7N, but not with other isomers of iso-HC_9H_7N.

Unlike 4-iso-HC_9H_7N, which shows overtones involving up to 10 quanta of ν_{48} (26 cm^{-1}, a″) in Fig. 6a, no significant contribution from higher-order overtones or their combination bands is predicted for the $D_1 \leftarrow D_0$ absorption spectrum of 8-iso-HC_9H_7N. Differences between harmonic vibrational frequencies of a specific normal mode in different electronic states serve as indicators of changes in the curvature of the potential energy surface along this normal coordinate near the equilibrium geometry. In Fig. S9 (SI), quotients $\nu_n(D_0)/\nu_n(D_1)$ for n = 1–48 are plotted for 4- and 8-iso-HC_9H_7N; $\nu_n(D_0)$ and $\nu_n(D_1)$ are vibrational wavenumbers of the nth vibrational mode in the

Table 4 Assignments of peaks in the fluorescence excitation spectrum of 4-iso-HC_9H_7N isolated in solid *para*-H_2

para-H_2	uB3PW91				
LIF[a]/cm^{-1}	FCHT[b]/cm^{-1}	Rel. int.[c]/%	Scaled[d]/cm^{-1}	Assignment	Sym.
	0	100	0	0_0^0	a′
48	51	29.6	(51)	48_0^2	a′
	102	13.1	(102)	48_0^4	a′
	153	6.5	(153)	48_0^6	a′
215	203	3.3	(204)	48_0^8	a′
		2.2	(228)	47_0^2	a′
		1.8	(255)	48_0^{10}	a′
338	336	1.8	336	32_0^1	a′
	528	2.0	(530)	$43_0^1 47_0^1$	a′
593	602	20.1	604	29_0^1	a′
655	653	5.9	(655)	$29_0^1 48_0^2$	a′
703	704	2.6	(706)	$29_0^1 48_0^4$	a′
751	755	8.1	755	27_0^1	a′
	806	2.4	(806)	$27_0^1 48_0^2$	a′
957	951	3.7	950	25_0^1	a′
1022	1025	5.4	1026	23_0^1	a′
1152	1150	3.2	1125	22_0^1	a′
		11.1	1151	20_0^1	a′
	1205	3.3	(1202)	$20_0^1 48_0^2$	a′
1250	1256	3.9	1357	18_0^1	a′
1304	1307	3.8	1299	17_0^1	a′
		3.7	1313	16_0^1	a′
		2.6	1335	15_0^1	a′
1410	1428	14.5	1428	11_0^1	a′
1498	1483	4.3	(1479)	$11_0^1 48_0^2$	a′
		1.8	1492	10_0^1	a′
	1534	1.9	(1530)	$11_0^1 48_0^4$	a′
		2.6	1532	9_0^1	a′
1620	1623	31.5	1624	8_0^1	a′
1700	1675	9.3	(1675)	$8_0^1 48_0^2$	a′
	1725	4.1	(1726)	$8_0^1 48_0^4$	a′
	1772	1.8	(1755)	$20_0^1 29_0^1$	a′
		2.0	(1777)	$8_0^1 48_0^6$	a′

[a] Vibrational spacing relative to the origin band at 18 495 cm^{-1} (540.7 nm). [b] Vibrational spacings from the convoluted simulated stick spectrum calculated with the FCHT method. [c] Intensities relative to the most intense peak (0_0^0 band). Only vibrational modes contributing with a relative intensity ≥1.5% are listed. [d] Harmonic vibrational wavenumbers scaled by a factor 0.978. Values given in parentheses for combination and overtone bands are the sum of the fundamentals.

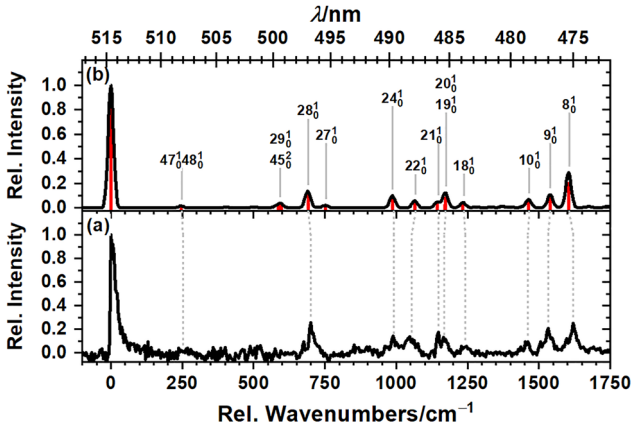

Fig. 7 Comparison of observed and simulated excitation of 8-iso-HC_9H_7N. (a) Fluorescence excitation spectrum of 8-iso-HC_9H_7N isolated in solid *para*-H_2 obtained by probing emission at 18 103–18 312 cm^{-1}. The bottom axis denotes the displacement from the orgin band, observed at 19 433 cm^{-1} (514.6 nm), whereas the top axis represents the wavelength of the observed spectrum. (b) The $D_1 \leftarrow D_0$ absorption spectrum simulated by convolution the Franck–Condon Herzberg–Teller stick spectrum (red) with a Gaussian line shape of FWHM 20 cm^{-1}; vibrational wavenumbers were scaled by 0.978. Vibrational mode assignments are indicated.

Table 5 Assignments of peaks in the fluorescence excitation spectrum of 8-iso-HC_9H_7N isolated in solid *para*-H_2

para-H_2	uB3PW91				
LIF[a]/cm^{-1}	FCHT[b]/cm^{-1}	Rel. int.[c]/%	Scaled[d]/cm^{-1}	Assignment	Sym.
	0	100	0	0_0^0	a′
252	246	1.4	(245)	$47_0^1 48_0^1$	a′
	591	2.0	587	29_0^1	a′
		1.9	(597)	45_0^2	a′
700	689	12.0	690	28_0^1	a′
	751	2.1	752	27_0^1	a′
992	986	9.8	986	24_0^1	a′
1055	1064	5.6	1065	22_0^1	a′
1148	1146	4.7	1143	21_0^1	a′
1169	1170	2.1	1169	20_0^1	a′
		7.9	1172	19_0^1	a′
1242	1232	4.0	1233	18_0^1	a′
1462	1463	6.2	1464	10_0^1	a′
1532	1537	9.6	1539	9_0^1	a′
1620	1604	19.7	1604	8_0^1	a′
	1674	0.7	(1676)	$24_0^1 28_0^1$	a′

[a] Vibrational spacing relative to the origin band at 19 433 cm^{-1} (514.6 nm). [b] Vibrational spacings from the convoluted simulated stick spectrum calculated with the FCHT method. [c] Intensities relative to the most intense peak (0_0^0 band). Only vibrational modes contributing with a relative intensity ≥1.5% are listed. [d] Harmonic vibrational wavenumbers scaled by a factor 0.978. Numbers given in parentheses for combination and overtone bands are the sum of the fundamentals.

D_0 and D_1 state, respectively. The significant reduction of ν_{48} from 56 to 26 cm^{-1} upon excitation from D_0 to D_1 of 4-iso-HC_9H_7N indicates a shallower potential energy surface for ν_{48} in the D_1 state, explaining the appearance of ν_{48} overtones and their combination bands in fluorescence excitation spectrum of 4-iso-HC_9H_7N.

3.5. Dispersed fluorescence and fluorescence excitation spectra of 5-iso-HC_9H_7N

Upon excitation at 495.5 nm (20 182 cm^{-1}) of a matrix of iso-C_9H_7N in solid *para*-H_2 deposited under electron bombardment, we observed additional emission features (system C) that could not be assigned to either 4- or 8-iso-HC_9H_7N, as illustrated in Fig. 2c and Fig. S5 (SI). Fluorescence emission probed in the range 580.9–587.6 nm (17 018–17 215 cm^{-1}) upon excitation at 18 688 cm^{-1} decays to <10% within 50 ns, *cf.* Fig. S10 (SI), suggesting an emission lifetime between those of 4- and 8-iso-HC_9H_7N, and, hence, the presence of a third distinct species.

Varying the excitation wavelength in increments of 0.1 nm while probing emission in the range 580.9–587.6 nm (17 018–17 215 cm^{-1}), as shown in Fig. S7 (SI), we obtained the fluorescence excitation spectrum depicted in Fig. 8a. The most intense feature is located at 18 688 cm^{-1} (535.1 nm), accompanied by sharp bands at 1502 (relative intensity 35%), 1161 (27%), 1063 (17%), 950 (17%), 847 (13%), 591 (20%), and 469 cm^{-1} (17%) above the most intense band. We compare this spectrum with the experimental fluorescence excitation spectra of 4- and 8-iso-HC_9H_7N isolated in solid *para*-H_2 and the simulated $D_1 \leftarrow D_0$ absorption spectra of various iso-HC_9H_7N isomers in Fig. S8 (SI). The second most intense feature (relative intensity ∼35%) in the simulated $D_1 \leftarrow D_0$ spectrum of 5-iso-HC_9H_7N, located near 1530 cm^{-1}, is consistent with the single intense experimental band near 1500 cm^{-1}. In contrast, in the simulated absorption spectra of all other isomers, this band is either shifted further to higher energies or accompanied by additional bands of comparable intensity. Furthermore, the observed spectral pattern in the range 400–1000 cm^{-1} is

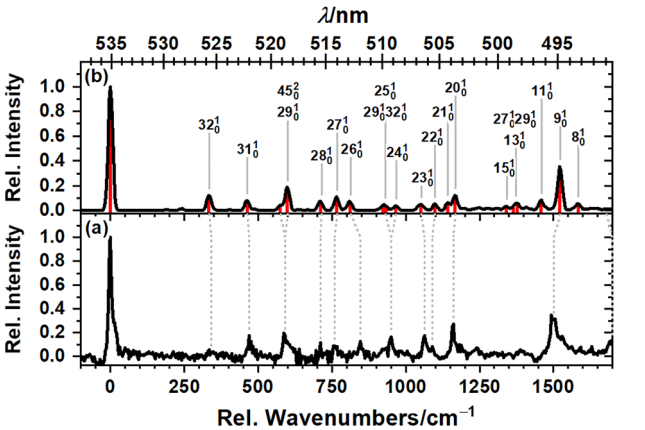

Fig. 8 Comparison of observed and simulated excitation spectra of 5-iso-HC_9H_7N. (a) Fluorescence excitation spectrum of 5-iso-HC_9H_7N isolated in solid *para*-H_2 obtained on probing emission in region 580.9–587.6 nm (17 018–17 215 cm^{-1}). The bottom axis denotes the displacement from the origin band, observed at 18 688 cm^{-1} (535.1 nm), whereas the top axis represents the wavelength of the observed spectrum. (b) The $D_1 \leftarrow D_0$ absorption spectrum simulated on convolution the simulated Franck–Condon Herzberg–Teller stick spectrum (red) with a Gaussian function with FWHM = 15 cm^{-1}; harmonic vibrational wavenumbers were scaled by 0.978. Vibrational mode assignments are indicated.

Table 6 Assignments of peaks in the fluorescence excitation spectrum of 5-iso-HC_9H_7N isolated in solid *para*-H_2

para-H_2	uB3PW91				
LIF[a]/cm^{-1}	FCHT[b]/cm^{-1}	Rel. int.[c]/%	Scaled[d]/cm^{-1}	Assignment	Sym.
	0	100.0	0	0_0^0	a′
341?	333	11.9	334	32_0^1	a′
469	462	8.1	462	31_0^1	a′
591	599	2.3	574	45_0^2	a′
		18.5	599	29_0^1	a′
711	712	4.9	711	28_0^1	a′
760	767	8.7	766	27_0^1	a′
847?	810	6.1	811	26_0^1	a′
950	927	2.2	923	25_0^1	a′
		1.9	933	$29_0^1 32_0^1$	a′
	966	2.3	966	24_0^1	a′
1063	1048	3.0	1050	23_0^1	a′
1090?	1099	2.9	1098	22_0^1	a′
	1142	5.7	1142	21_0^1	a′
1161	1166	10.7	1167	20_0^1	a′
	1342	2.5	1340	15_0^1	a′
	1377	1.6	1365	$27_0^1 29_0^1$	a′
		3.8	1378	13_0^1	a′
	1459	6.8	1458	11_0^1	a′
1502	1522	33.6	1522	9_0^1	a′
	1584	4.2	1585	8_0^1	a′

[a] Vibrational spacings relative to the origin band at 18 688 cm^{-1} (535.1 nm). Tentatively assigned peaks are marked with ?. [b] Vibrational spacings from the convoluted simulated stick spectrum calculated with the FCHT method. [c] Intensities relative to the most intense peak (0_0^0 band). Only vibrational modes contributing with a relative intensity ≥1.5% are listed. [d] Harmonic vibrational wavenumbers scaled by a factor 0.978. Values given in parentheses for combination and overtone bands are the sum of the fundamentals.

satisfactorily reproduced by simulation, with the exception of the lowest-energy feature at ∼335 cm^{-1}, which is predicted but only tentatively identified in the experimentally spectrum due to its small intensity.

Vibrational assignments derived from a comparison to the simulated absorption spectrum of 5-iso-HC_9H_7N are indicated in Fig. 8b and listed in Table 6; the agreement between experiment and FCHT calculation is satisfactory, with an average absolute deviation of 13 ± 11 cm^{-1}. This deviation is slightly larger than those of 4- and 8-iso-HC_9H_7N, presumably because of the lower signal-to-noise ratio due to small fluorescence emission intensity and the likely interference due to emission from other isomers as indicated in Fig. S7 (SI).

Following the above discussion, we assign the fluorescence excitation spectrum depicted in Fig. 8a to the $D_1 \leftarrow D_0$ absorption of 5-iso-HC_9H_7N. Similar to the fluorescence excitation spectrum of 8-iso-HC_9H_7N, the fluorescence excitation spectrum of 5-iso-HC_9H_7N is composed nearly exclusively of fundamental vibrational modes of a′ symmetry.

As demonstrated in Fig. S11 (SI), except for the origin band, the fluorescence excitation spectrum of 5-iso-HC_9H_7N overlaps significantly with those of 4- and 8-iso-HC_9H_7N. Due to these similarities, identifying an excitation band other than the origin band that yields an interference-free dispersed fluorescence spectrum of 5-iso-HC_9H_7N is particularly challenging. The pure dispersed fluorescence spectrum of 5-iso-HC_9H_7N isolated in solid *para*-H_2, depicted in Fig. 9a, was acquired upon excitation at the 0_0^0 band (18 688 cm^{-1}). Consequently, the spectrum close to the 0_0^0 band is strongly interfered by the excitation laser, and the experimental spectrum depicted in Fig. 9, therefore, only covers the energy region well below the excitation energy. Nevertheless, a comparison of the spectral structure above 1000 cm^{-1} with the simulated $D_1 \rightarrow D_0$ emission spectra, Fig. 2 and 9b strongly supports our assignment of the recorded spectrum to the 5-iso-HC_9H_7N radical.

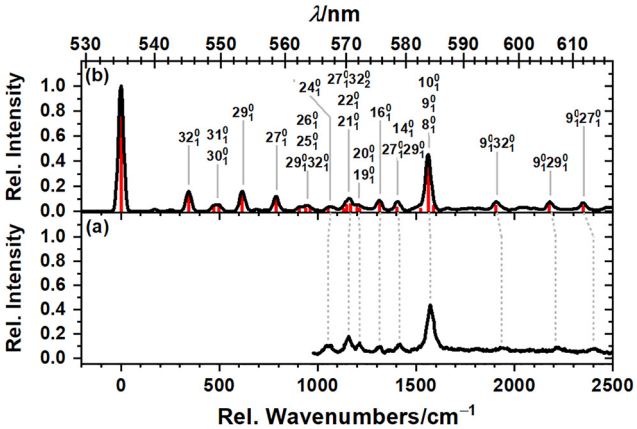

Fig. 9 Comparison of observed and simulated dispersed fluorescence spectra of 5-iso-HC_9H_7N. (a) Partial dispersed fluorescence spectrum of 5-iso-HC_9H_7N isolated in solid *para*-H_2 recorded upon excitation at 18 688 cm^{-1} (535.1 nm). The bottom axis denotes the displacement from the origin band, observed at 18 688 cm^{-1}, whereas the top axis represents the wavelength of the observed spectrum. And (b) The $D_1 \rightarrow D_0$ emission spectrum simulated by convolution the Franck–Condon Herzberg–Teller stick spectrum (red) with a Gaussian line shape of FWHM 30 cm^{-1}; vibrational wavenumbers were scaled by 0.978. Vibrational mode assignments are indicated.

Peak positions inferred from the partial dispersed fluorescence spectrum in Fig. 9a and their assignments derived by comparison to the simulated $D_1 \rightarrow D_0$ emission spectrum of 5-iso-HC_9H_7N are presented in Table 7, together with the IR absorption lines reported by Joshi *et al.*[30] The most intense feature at 1571 cm^{-1} is assigned to the 9_1^0 transition, with partial overlap from weaker bands of 10_1^0 and 8_1^0. Five additional features below 1500 cm^{-1} were identified; these show satisfactory agreement with FCHT predictions. Three weak features above 1900 cm^{-1} are tentatively assigned to combination bands involving ν_9 and ν_{27}, ν_{29}, or ν_{32} because of their small intensities. Within the spectral range covered, simulated and experimental peak positions for fundamental vibrational modes exhibit an average absolute deviation of 6 ± 4 cm^{-1}. When the weak combination bands are included, the average absolute deviation increases to 14 ± 15 cm^{-1}.

Joshi *et al.*[30] reported five IR absorption lines below 2500 cm^{-1} for 5-iso-HC_9H_7N isolated in solid *para*-H_2: three a″ symmetric vibrations ν_{42}, ν_{41}, and ν_{39}, which are not expected to contribute to the dispersed fluorescence spectrum, and the two a′ symmetric vibrations ν_{20} and ν_{13}, which are predicted to appear in the emission spectrum with relative intensities of 2.6 and 1.3%, respectively. The ν_{20} band, which

Table 7 Assignments of peaks in the dispersed fluorescence spectrum of 5-iso-HC_9H_7N isolated in solid *para*-H_2

para-H_2		uB3PW91				
IR[a]/ cm^{-1}	LIF[b]/ cm^{-1}	FCHT[c]/ cm^{-1}	Rel. int.[d]/ %	Scaled[e]/ cm^{-1}	Assignment	Sym.
		0	100.0	0	0_0^0	a′
		344	11.3	345	32_1^0	a′
		493	3.4	471	31_1^0	a′
			4.2	499	30_1^0	a′
		618	15.1	617	29_1^0	a′
(652.3)			(<0.1)	645	42_1^0	a″
(708.6)			(<0.1)	712	41_1^0	a″
		786	8.4	787	27_1^0	a′
(821.9)			(<0.1)	821	39_1^0	a″
		943	3.0	906	26_1^0	a′
			2.4	938	25_1^0	a′
			2.3	(962)	$29_1^0 32_1^0$	a′
	1054	1060	2.5	1052	24_1^0	a′
	1158	1158	1.6	(1132)	$27_1^0 32_1^0$	a′
			4.7	1148	22_1^0	a′
			5.5	1167	21_1^0	a′
1201.3	1211	1205	2.6	1198	20_1^0	a′
			1.6	1213	19_1^0	a′
	1314	1314	8.2	1314	16_1^0	a′
	1415	1404	2.8	1404	14_1^0	a′
			1.8	(1404)	$27_1^0 29_1^0$	a′
(1402.0)			(1.3)	1406	13_1^0	a′
	1571	1561	1.9	1522	10_1^0	a′
			42.3	1561	9_1^0	a′
			4.1	1587	8_1^0	a′
	1934?	1905	4.2	(1906)	$9_1^0 32_1^0$	a′
	2210?	2179	5.7	(2177)	$9_1^0 29_1^0$	a′
	2403?	2347	3.6	(2348)	$9_1^0 27_1^0$	a′

[a] Peak positions in the IR absorption spectrum of 5-iso-HC_9H_7N isolated in solid *para*-H_2 reported by Joshi *et al.*[30] Lines in parentheses represent modes predicted by FCHT simulations with a relative intensity of <1.5%. [b] Vibrational spacing relative to the origin band at 18 668 cm^{-1} (535.1 nm) in the fluorescence excitation spectrum of 5-iso-HC_9H_7N. Tentatively assigned peaks are marked with ?. [c] Vibrational spacings from the convoluted simulated stick spectrum calculated with the FCHT method. [d] Intensities relative to the most intense peak (0_0^0 band). Only vibrational modes with relative intensities ≥1.5% are listed. The weak features corresponding to IR absorption bands reported by Joshi *et al.*[30] are listed in parentheses. [e] Harmonic vibrational wavenumbers scaled by a factor 0.978. Values given in parentheses for combination and overtone bands are the sum of the fundamentals.

overlaps with ν_{19}, was observed in the dispersed fluorescence spectrum, whereas the ν_{13} band was too weak to be positively identified.

For the three C–N and C–C stretching modes ν_{10}, ν_9, and ν_8, as previously discussed for 4- and 8-iso-HC_9H_7N, calculations predict relative intensities of 1.9, 42.3, and 4.1%, respectively. Atomic displacement vectors associated with these vibrations and the geometry changes induced by the electronic transition between D_1 and D_0 are illustrated in Fig. S12 (SI). The electronic transition strongly affects the bond lengths of the C–N and the central C(4a)–C(8a) bond, consistent with the large Franck–Condon factor calculated for mode ν_9. In contrast, modes ν_8 and ν_{10} exert only minor impact on these two bonds.

Of the eight iso-HC_9H_7N isomers previously identified in solid *para*-H_2 by IR spectroscopy, only the dispersed fluorescence and fluorescence excitation spectra of the three low-energy isomers 4-, 5-, and 8-iso-HC_9H_7N were observed. The lowest-energy isomer, iso-C_9H_7NH, although reported as the most abundant in the study by Joshi *et al.*,[30] was not observed. TD-DFT calculations predict the lowest-energy electronic transition of iso-C_9H_7NH at 839.58 nm (11 911 cm^{-1}, vertical excitation, Table 1), which is beyond the detection range of our iCCD. Moreover, with a predicted oscillator strength of 0.001 and a vertical emission wavelength of 2268 nm, detecting the weak fluorescence emission of iso-C_9H_7NH is expected to be challenging. Another low-lying isomer, 1-iso-HC_9H_7N with relative energy +6 kJ mol^{-1}, was also not observed, likely because the transition is predicted to have a low fluorescence yield (f = 0.001). Furthermore, the D_1–D_0 electronic transition induces a significant out-of-plane distortion of the molecule (Fig. S1, SI), resulting in a small Franck–Condon overlap between these two states and a vertical emission wavelength of 1180 nm, which is beyond our detection limit. Of the three high-energy isomers, 3-, 6-, and 7-iso-HC_9H_7N, Joshi *et al.*[30] only observed 6-iso-HC_9H_7N in experiments on iso-C_9H_7N/*para*-H_2 matrices deposited under electron bombardment. For this isomer, our TD-DFT calculations predict a vertical emission energy of 592.8 nm and oscillator strength of 0.005. The small oscillator strength and expected low concentration of this high energy isomer make the detection unlikely.

The positions of the vibrationless transitions inferred from the fluorescence spectra of the three experimentally observed iso-HC_9H_7N isomers differ substantially from the predicted vertical excitation energies listed in Table 1. For hybrid functionals such as B3LYP and B3PW91, TD-DFT benchmark studies typically indicate mean absolute deviations of 0.3–0.5 eV in excitation energies, either between TD-DFT and experimental data or between TD-DFT and higher-level *ab initio* calculations.[37,38]

These benchmark studies, however, primarily concern only singlet and triplet transitions of closed-shell molecules and rarely address doublet–doublet transitions of open-shell species. As doublet states are often subject to spin-contamination and exhibit significant multi-reference character, which are in most cases not captured adequately by TD-DFT, uncertainties in excitation energies for doublet–doublet transitions are expected to be larger. The mean absolute deviation of 0.46 eV between computed vertical excitation energies and experimentally determined 0_0^0 band positions for the three iso-HC_9H_7N isomers isolated in solid *para*-H_2 therefore appears reasonable. According to our experimental results, the D_1–D_0 energy gap increases in the order 4-iso-HC_9H_7N < 5-iso-HC_9H_7N < 8-iso-HC_9H_7N. TD-DFT calculations predict the highest D_1–D_0 excitation energy for 8-iso-HC_9H_7N, in agreement with our experimental findings, but an inverted order for 4- and 5-iso-HC_9H_7N with a minor difference of only ∼1 nm from calculations.

3.6 Hydrogenated iso-quinolines as potential DIB carriers

The most prominent features in the fluorescence excitation spectra of 4-, 5-, and 8-iso-HC_9H_7N isolated in solid *para*-H_2 are located at 540.8, 535.1, and 514.7 nm, respectively; other

features are comparatively weak. Within this wavelength range, Hobbs *et al.*[39] reported a DIB density of ~17 DIB per 20 nm from observations of HD 204827. Unfortunately, electronic absorption spectra of hydrogenated PAH and PANH in the gas phase have rarely been reported, and matrix shifts for electronic transitions of these open-shell species isolated in solid *para*-H_2 are not fully understood. For 1-$HC_{10}H_8$, a red-shift of 86 cm^{-1} was observed for the D_1–D_0 transition located at 18 881 cm^{-1} in solid *para*-H_2,[24] aligning with the average matrix shift of 70 ± 28 cm^{-1} derived from available data for PAH containing up to 42 carbon atoms and their protonated and hydrogenated derivative isolated in solid *para*-H_2.[25] Adopting this average matrix shift, we estimate positions of the D_1–D_0 0_0^0 bands of gaseous 4-, 5-, and 8-iso-HC_9H_7N to be 539.5–537.9 nm, 533.9–532.4 nm, and 513.6–512.1 nm, respectively. A detailed comparison of the experimental fluorescence excitation spectra with the overall DIB spectrum reported by Jennsikens and Désert[40] is shown in Fig. S13 (SI).

In their DIB catalogue based on observations of six stars characterised by varying degrees of reddening, Jenniskens and Désert[40] list four ''certain'' DIB in the range 510–545 nm: at 510.970, 536.214, 536.360, and 540.456 nm. The first three lie clearly outside the range of the transitions observed in this work; a matrix red shift of ≥140 cm^{-1} would be required to map our experimental data onto these line positions, substantially larger than the average shift typically observed for PAH in solid *para*-H_2. The final DIB at 540.456 nm (18 503.89 cm^{-1}) is located ~10 cm^{-1} higher in energy than the observed D_1–D_0 transition of 4-iso-HC_9H_7N in solid *para*-H_2 at 18 492 cm^{-1}. However, after applying the average matrix shift of 70 ± 28 cm^{-1} to our experimental transition wavelength, the corrected gas-phase transition for 4-iso-HC_9H_7N becomes ~60 cm^{-1} higher in energy than the DIB band, rendering a contribution of 4-iso-HC_9H_7N to the DIB spectrum unlikely. This is consistent with astrochemical models predicting that small PAH (containing less than 40 C atoms) are not stable under the conditions of the ISM. Pursuing electronic absorption spectra of larger PAH/PANH is hence desirable.

4. Conclusions

This study reports the previously unobserved dispersed fluorescence and fluorescence excitation spectra of three hydrogenated iso-quinoline isomers: 4-, 5-, and 8-iso-HC_9H_7N. Upon deposition of a mixture of iso-C_9H_7N and *para*-H_2 under electron bombardment and subsequent irradiation at wavelengths <540 nm, we observed three distinct fluorescence emission progressions originating at 18 492, 18 688, and 19 430 cm^{-1}, with characteristic emission lifetimes of ~6, <50, and ~105 ns, respectively. These transitions were assigned to the $D_1 \rightarrow D_0$ transitions of 4-, 5-, and 8-iso-HC_9H_7N, based on comparison of the recorded spectra with spectra simulated by a Franck–Condon Herzberg–Teller approach. The experimental excitation spectra of these three isomers also agree satisfactorily with the corresponding simulated absorption spectra. Dispersed fluorescence and fluorescence excitation spectra associated with the D_1–D_0 transition of all three isomers are dominated by vibrational normal modes of a′ symmetry, with the 0_0^0 band as the most intense feature. Vibrational modes inferred from the dispersed fluorescence spectra are distinctively different from those observed in the IR absorption spectra previously reported by Joshi *et al.*[30] Differences in relative intensities and the contribution of overtone and combination bands are discussed in relation to changes in geometries and in the vibrational potential energy surfaces between the D_0 and D_1 states. Based on the observed spectral positions and expected matrix shifts, a contribution of electronic bands of 4-, 5- and 8-iso-HC_9H_7N to the DIB appears unlikely.

Conflicts of interest

There are no conflicts to declare.

Data availability

The data supporting this article have been included as part of the supplementary information (SI). Supplementary information: variation of vibronic pattern as function of the position of H-addition. Tables: Scaled harmonic vibrational wavenumbers of the D_0 and D_1 state of the eight most stable isomers of iso-HC_9H_7N. Figures: Optimized geometry of the D_1 state of 1-iso-HC_9H_7N. Simulated $D_1 \rightarrow D_0$ emission spectrum of 1-iso-HC_9H_7N. Characteristic displacements induced by modes ν_{29}, ν_{30}, ν_{31}, and ν_{32}. Geometry changes induced by the D_1–D_0 transition for *n*-iso-HC_9H_7N (*n* = 3–8). Partial dispersed fluorescence spectrum upon excitation at 497.0, 475.0, and 495.5 nm. Temporal behaviour of fluorescence emission of 4-, 8-, and 5-iso-HC_9H_7N. Relative changes of bond length and angles upon electronic transition between D_0 and D_1 for 4- and 8-iso-HC_9H_7N. Normalised dispersed fluorescence and fluorescence excitation spectra of 4-, 5-, and 8-iso-HC_9H_7N isolated in solid *para*-H_2. Quotients of vibrational wavenumbers of the D_0 and D_1 state for 4- and 8-iso-HC_9H_7N. Comparison of observed fluorescence excitation spectra with simulated $D_1 \leftarrow D_0$ spectra of various iso-HC_9H_7N isomers. Changes in optimized geometries of 5-iso-HC_9H_7N upon transition between D_0 and D_1 and atom displacements induced by modes ν_8, ν_9, and ν_{10}. Comparison of the fluorescence excitation spectra of 4-, 5-, and 8-iso-HC_9H_7N to the DIB spectrum. See DOI: **https://doi.org/10.1039/d5cp03455h**.

Acknowledgements

This work was supported by National Science and Technology Council, Taiwan (grants NSTC113-2639-M-A49-002-ASP), Center for Emergent Functional Matter Science of National Yang Ming Chiao Tung University from The Featured Areas Research Center Program within the framework of the Higher Education Sprout Project by the Ministry of Education (MOE) in Taiwan, and the EU's Horizon Europe program MSCA

(ActBio, No. 101107213) and COST Action (CA21101 "COSY"). The National Center for High-Performance Computing (NCHC) of National Applied Research Laboratories (NARLabs) in Taiwan and the computer facilities of the Scuola Normale Superiore, Italy, provided computer time. We thank Prof. Julien Bloino for fruitful discussions and access to the Gaussian development version.

References

1 M. L. Heger, *Lick Obs. Bull.*, 1922, **10**, 141–145.
2 R. Vogrinčič, J. Kos, T. Zwitter, G. Traven, K. L. Beeson, K. Čotar, U. Munari, S. Buder, S. L. Martell and G. F. Lewis, *et al.*, *Mon. Not. R. Astron. Soc.*, 2023, **521**, 3727–3748.
3 H. Fan, L. M. Hobbs, J. A. Dahlstrom, D. E. Welty, D. G. York, B. Rachford, T. P. Snow, P. Sonnentrucker, N. Baskes and G. Zhao, *Astrophys. J.*, 2019, **878**, 151.
4 P. Sonnentrucker, B. York, L. M. Hobbs, D. E. Welty, S. D. Friedman, J. Dahlstrom, T. P. Snow and D. G. York, *Astrophys. J., Suppl. Ser.*, 2018, **237**, 40.
5 E. K. Campbell, M. Holz, D. Gerlich and J. P. Maier, *Nature*, 2015, **523**, 322–323.
6 E. K. Campbell, M. Holz, J. P. Maier, D. Gerlich, G. A. H. Walker and D. Bohlender, *Astrophys. J.*, 2016, **822**, 17.
7 N. L. J. Cox, *EAS Publ. Ser.*, 2011, **46**, 349–354.
8 M. K. Crawford, A. G. G. M. Tielens and L. J. Allamandola, *Astrophys. J.*, 1985, **293**, L45.
9 J. L. Puget, A. Leger and F. Boulanger, *Astron. Astrophys.*, 1985, **142**, L19–L22.
10 L. J. Allamandola, A. G. G. M. Tielens and J. R. Barker, *Astrophys. J.*, 1985, **290**, L25–L28.
11 A. G. G. M. Tielens, *Annu. Rev. Astron. Astrophys.*, 2008, **46**, 289–337.
12 C. M. Canelo, A. C. S. Friaça, D. A. Sales, M. G. Pastoriza and D. Ruschel-Dutra, *Mon. Not. R. Astron. Soc.*, 2018, **475**, 3746–3763.
13 D. M. Hudgins, J. C. W. Bauschlicher and L. J. Allamandola, *Astrophys. J.*, 2005, **632**, 316–332.
14 A. Ricca, C. Boersma and E. Peeters, *Astrophys. J.*, 2021, **923**, 202.
15 P. G. Stoks and A. W. Schwartz, *Geochim. Cosmochim. Acta*, 1982, **46**, 309–315.
16 P. G. Stoks and A. W. Schwartz, *Geochim. Cosmochim. Acta*, 1981, **45**, 563–569.
17 M. E. Jacox, *J. Mol. Struct.*, 1987, **157**, 43–59.
18 C. Crépin and A. Tramer, *Chem. Phys.*, 2001, **272**, 227–241.
19 M. Bahou, P. Das, Y.-F. Lee, Y.-J. Wu and Y.-P. Lee, *Phys. Chem. Chem. Phys.*, 2014, **16**, 2200–2210.
20 M. Bahou, C.-W. Huang, Y.-L. Huang, J. Glatthaar and Y.-P. Lee, *J. Chin. Chem. Soc.*, 2010, **57**, 771–782.
21 M. Tsuge, C.-Y. Tseng and Y.-P. Lee, *Phys. Chem. Chem. Phys.*, 2018, **20**, 5344–5358.
22 I. Weber and Y.-P. Lee, *J. Phys. Chem. A*, 2024, **128**, 4984–4991.
23 I. Weber, M. Tsuge, P. Sundararajan, M. Baba, H. Sakurai and Y.-P. Lee, *J. Phys. Chem. A*, 2022, **126**, 5283–5293.
24 I. Weber, C.-W. Wang, S.-C. Huang, C.-Y. Zhu and Y.-P. Lee, *J. Phys. Chem. A*, 2022, **126**, 8423–8433.
25 I. Weber, P. R. Joshi, D. T. Anderson and Y.-P. Lee, *J. Phys. Chem. Lett.*, 2024, **15**, 11361–11373.
26 E. Plazas, M. C. Avila M, D. R. Muñoz and L. E. Cuca S, *Pharmacol. Res.*, 2022, **177**, 106126.
27 S. P. Verevkin, S. P. Safronov, A. A. Samarov and S. V. Vostrikov, *Appl. Sci.*, 2021, **11**, 11758.
28 S. P. Safronov, S. V. Vostrikov, A. A. Samarov and S. P. Verevkin, *Fuel*, 2022, **317**, 123501.
29 H. Harb, S. N. Elliott, L. Ward, I. T. Foster, S. J. Klippenstein, L. A. Curtiss and R. S. Assary, *Digital Discovery*, 2023, **2**, 1813–1830.
30 P. R. Joshi, M. Tsuge, C.-Y. Tseng and Y.-P. Lee, *Phys. Chem. Chem. Phys.*, 2023, **25**, 11934–11950.
31 S.-C. Huang and Y.-P. Lee, *Chem. Phys. Lett.*, 2016, **665**, 53–58.
32 M. J. Frisch, G. W. Trucks, H. B. Schlegel, G. E. Scuseria, M. A. Robb, J. R. Cheeseman, G. Scalmani, V. Barone, G. A. Petersson and H. Nakatsuji, *et al.*, *Gaussian 16 Rev. B.01*, Gaussian Inc., Wallingford CT, 2016.
33 A. Baiardi, J. Bloino and V. Barone, *J. Chem. Theory Comput.*, 2013, **9**, 4097–4115.
34 J. Bloino, A. Baiardi and M. Biczysko, *Int. J. Quantum Chem.*, 2016, **116**, 1543–1574.
35 Q. Yang, M. Fusè, J. Bloino and V. Barone, *Spectrochim. Acta, Part A*, 2021, **254**, 119631.
36 J. C. Dobrowolski and P. F. J. Lipiński, *RSC Adv.*, 2016, **6**, 23900–23904.
37 I. Knysh, F. Lipparini, A. Blondel, I. Duchemin, X. Blase, P.-F. Loos and D. Jacquemin, *J. Chem. Theory Comput.*, 2024, **20**, 8152–8174.
38 J. Liang, X. Feng, D. Hait and M. Head-Gordon, *J. Chem. Theory Comput.*, 2022, **18**, 3460–3473.
39 L. M. Hobbs, D. G. York, T. P. Snow, T. Oka, J. A. Thorburn, M. Bishof, S. D. Friedman, B. J. McCall, B. Rachford and P. Sonnentrucker, *et al.*, *Astrophys. J.*, 2008, **680**, 1256–1270.
40 P. Jenniskens and F.-X. Désert, *Astron. Astrophys., Suppl. Ser.*, 1994, **106**, 39–78.